ACS OMEGA

Open Access

This article is licensed under CC-BY-NC-ND 4.0

http://pubs.acs.org/journal/acsodf

Article

Investigating the Antibacterial and Anti-inflammatory Potential of Polyol-Synthesized Silver Nanoparticles

Ibrar Ahmad, Muhammad Nadeem Khan, Khizar Hayat, Tanveer Ahmad, Dilawar Farhan Shams, Waliullah Khan, Vineet Tirth, Gauhar Rehman, Wazir Muhammad, Muawya Elhadi, Afraa Alotaibi, and Said Karim Shah*

Cite This: *ACS Omega* 2024, 9, 13208−13216

Read Online

ACCESS | Metrics & More | Article Recommendations | Supporting Information

ABSTRACT: Silver nanoparticles (Ag-NPs) were synthesized by using the polyol method. The structural and morphological characteristics of Ag-NPs were studied by using X-ray diffraction (XRD) and field-emission scanning electron microscopy (FE-SEM). The XRD analysis revealed the formation of single-phase polycrystalline Ag-NPs with an average crystallite size and lattice constant of ∼23 nm and 4.07 Å, respectively, while the FE-SEM shows the formation of a uniform and spherical morphology. Energy-dispersive X-ray spectroscopy confirmed the formation of single-phase Ag-NPs, and no extra elements were detected. A strong absorption peak at ∼427 nm was observed in the UV−vis spectrum, which reflects the surface plasmon resonance (SPR) behavior characteristic of Ag-NPs with a spherical morphology. Fourier-transform infrared (FTIR) spectra also supported the XRD and EDX results with regard to the purity of the prepared Ag-NPs. Anti-inflammatory activity was tested using HRBCs membrane stabilization and heat-induced hemolysis assays. The antibacterial activity of Ag-NPs was evaluated against four different types of pathogenic bacteria by using the disc diffusion method (DDM). The Gram-negative bacterial strains used in this study are *Escherichia coli* (*E. coli*), Klebsiella, Shigella, and Salmonella. The analysis suggested that the antibacterial activities of Ag-NPs have an influential role in inhibiting the growth of the tested Gram-negative bacteria, and thus Ag-NPs can find a potential application in the pharmaceutical industry.

INTRODUCTION

Applications of nanotechnology have practically impacted all aspects of modern life. For a couple of decades, the synthesis of nanostructures has attracted significant attention due to their potential uses in various fields, including optoelectronics,[1,2] catalysis,[3,4] sensing,[5−7] water purification,[8−11] nanomedicine,[12−14] efficient antimicrobial agents,[15,16] etc. Silver nanoparticles (Ag-NPs) have received more attention than other noble metal nanostructures as efficient antimicrobial agents against different Gram-positive and Gram-negative bacterial strains. It is evident from previous research articles that in the case of utilizing metal nanoparticles for antibacterial activities, one of the essential factors is the control of uniform size and morphology at the nanoscale. Several research groups have reported novel synthetic routes for silver nanostructures. Song et al. reported that silver nanostructures' morphology significantly controls the surface plasmon resonance (SPR) effect.[17] Furthermore, in the literature, various kinds of morphologies have been reported, such as nanoprisms,[18] nanodisks,[19] nanorods,[20] nanowires,[21] nanospheres,[22] nanoflowers,[23] etc., to explore the size-dependent electronic and optical properties of silver metal. These different kinds of morphologies of silver are tested against biological activities using a wide range of microorganisms, including bacteria,[24] fungi,[25] viruses,[26] etc. It was found that silver has suitable antimicrobial activities, and more importantly, silver is not toxic to humans or the environment. Owing to its nontoxic nature and efficient biological activities, silver has been widely used in some medicines, especially anti-inflammatory drugs,[27] textiles,[28] and food and water processing.[29] The body responds to infection or injury through a complex process known as inflammation, characterized by reddening, swelling, and pain in the affected area. Unregulated inflammation can result in chronic inflammation, which can lead to mutations and DNA damage, ultimately resulting in the growth of cancer cells.[30] Anti-inflammatory drugs are administered to mitigate the harmful effects of reactive oxygen species (ROS) and inflammation. Steroids and nonsteroidal anti-inflammatory drugs (NSAIDs) are usually used to treat inflammation. NSAIDs are effective at reducing inflammation by inhibiting enzymes. These medications some time can lead to imbalances

Received: December 13, 2023
Revised: February 23, 2024
Accepted: February 27, 2024
Published: March 9, 2024

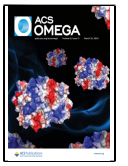

© 2024 The Authors. Published by American Chemical Society

in electrolyte and water levels within the body, which may also result in damage to the cardiovascular, liver, and renal systems.[31] To ensure treatment safety, drugs with no side effects are used to alleviate inflammation. Therefore, human red blood cell (HRBC) membrane stabilization was used to evaluate the in vitro anti-inflammatory activity of the Ag-NPs. The rapid development of antibiotic resistance in microorganisms has increased the need for alternative antimicrobial agents. Therefore, Ag-NPs have emerged as a promising alternative for antibiotic resistance in microorganisms. However, the mechanism of action of Ag-NPs against bacteria has yet to be elucidated. Although the antibacterial activity of Ag-NPs is explained by several hypotheses,[32] one of the critical mechanisms by which Ag-NPs exert their antimicrobial activity is the release of silver ions (Ag^+). These ions disrupt the structure and function of the microbial cell membrane, leading to the cell's death.[33,34] Moreover, the excellent surface-to-volume ratio of Ag-NPs leads to their fast chemical reactivity, followed by the formation of ROS within bacterial cells, resulting in rapid cell death as shown in Supporting Information Figure S1.1. The concentration, morphology, and size of Ag-NPs highly influence their antibacterial activities.[35−38] Overall, Ag-NPs have demonstrated excellent antimicrobial activity against a wide range of microorganisms and have the potential to be utilized as alternatives to traditional antimicrobial agents. Further research is needed to fully understand their mechanisms of action and optimize their use in various applications. Therefore, in this study, we report the synthesis of highly monodispersed Ag-NPs via a polyol method in which the particle size and morphology of Ag-NPs are controlled by ethylene glycol, polyvinylpyrrolidone, and some experimental parameters. Furthermore, results regarding investigating the antibacterial activity of Ag-NPs with different concentrations against *Escherichia coli*, Klebsiella, Shigella, and Salmonella Gram-negative bacteria are also reported and discussed.

MATERIALS AND EXPERIMENTAL DETAILS

Silver nitrate ($AgNO_3$, purity ≥ 98.8%), polyvinylpyrrolidone [$(C_6H_9NO)_n$, M_w ∼ 1300k], and ethylene glycol ($C_2H_6O_2$, purity ≥ 99.0%) were purchased from Sigma-Aldrich and were used without further purification for the synthesis of Ag-NPs. Phosphate buffered saline (pH ∼ 7.4, Sigma-Aldrich), distilled water, NaCl, human blood, and diclofenac sodium were used in heat-induced hemolysis assay and HRBC-membrane stabilization.

The polyol synthesis approach synthesized uniform and homogeneously dispersed spherical-shaped Ag-NPs. Briefly, 20 mL of ethylene glycol (solvent and reducing agent) was taken in a round-bottom flask placed in an oil bath. Then, 1 g of PVP was added to EG and stirred vigorously for around 20 min at 120 °C. A separate solution of $AgNO_3$ of 0.25 g in 10 mL EG was prepared and then added dropwise to the PVP solution and placed in an oil bath. This mixture was kept at the same temperature in an oil bath for 90 min under stirring at 450 rpm. After reaction completion, the solution was centrifuged at 12,000 rpm and rinsed several times with deionized water (DI) and ethanol, followed by drying in the oven overnight at 60 °C. This whole synthesis procedure is summarized in the schematic diagram, as shown in Figure 1.

Antibacterial Activities. The ability of Ag-NPs to interact with the cellular membranes of different types of bacterial strains can be harnessed to determine their antibacterial

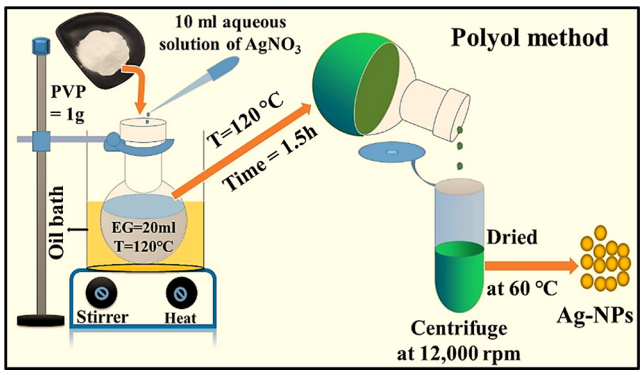

Figure 1. Schematic showing the polyol method used for the synthesis of Ag-NPs.

efficiency. The robust interactions between Ag^+ and proteins as well as lipids encourage alterations in the osmotic equilibrium, leading to a direct augmentation of membrane permeability. Further, these ions disrupt the structure and function of the microbial cell membrane, leading to the cell's death. Therefore, the antibacterial activities of Ag-NPs against four different types of pathogenic Gram-negative bacterial strains (*E. coli*, Klebsiella, Shigella, and Salmonella) and two different antibiotics (ciprofloxacin and ceftriaxone) were determined using the disc diffusion method (DDM). The prepared plates were inoculated under aseptic conditions at 37 °C for 24 h, and the growth inhibition zone's diameter was measured after the incubation period and compared with the effect of antibiotics against these bacterial strains.

In Vitro Anti-inflammatory Activities. To investigate the in vitro anti-inflammatory activity of the prepared Ag-NPs, human RBC (HRBC) membrane stabilization and heat-induced hemolysis assays were conducted. Lysosomal enzymes are released during inflammation, which causes various inflammation-associated diseases. Degeneration of the lysosomal membrane is inhibited by anti-inflammatory drugs. The compositions of lysosomes and the HRBC-membrane were the same. Therefore, in this work, the HRBC membrane stabilization potential of Ag-NPs was tested by preventing the decomposition of red blood cell membranes mediated by hypotonicity.

Suspension Preparation for HRBC Membrane Stabilization. Fresh human blood, approximately 5 mL, was collected from a healthy individual who had refrained from using steroids for 2 weeks before the experiment. Blood samples were obtained from humans by using EDTA tubes and then centrifuged at 3000 rpm for ∼20 min. The resulting supernatant was removed, and the RBC was washed with an isotonic saline solution. The process of centrifugation and washing was repeated five times to obtain a clear supernatant. Steps (a), (b), and (c) were used to prepare the reaction mixture for the control, standard, and test samples: a pellet having HRBCs was added to make a 10% suspension in an isotonic saline solution.

(a) Control reaction mixture: This contained 0.5 mL of a 10% suspension of HRBC in isotonic NaCl solution, 1 mL of PBS (∼0.25% w/v and NaCl solution), and 1 mL of isotonic saline (∼0.85% w/v and NaCl solution).
(b) Standard reaction mixture: This contained 0.5 mL of the same HRBC suspension, 1 mL of PBS, 2 mL of hypotonic NaCl solution (∼0.25% w/v and NaCl

https://doi.org/10.1021/acsomega.3c09851
ACS Omega 2024, 9, 13208−13216

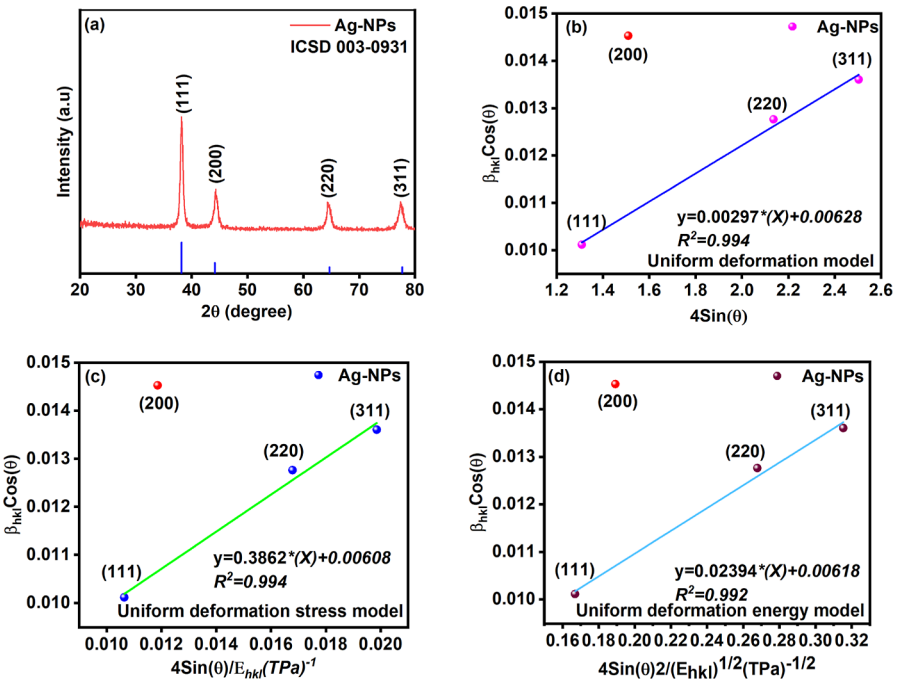

Figure 2. (a) XRD pattern and standard ICSD card #: 003-0931, (b) UDM, (C) UDSM, and (d) UDEDM W−H plot of Ag-NPs.

solution), 1 mL of isotonic NaCl solution, and 1 mL of different concentrations of diclofenac sodium (1 mg/mL).

(c) Test samples reaction mixture group: This contained 0.5 mL of HRBC suspension, 1 mL of different concentrations (20, 40, 60, and 80 μg/mL) of the prepared Ag-NPs, 1 mL of PBS, 2 mL of hypotonic NaCl solution, and 1 mL of isotonic NaCl.

The reaction mixtures were then incubated for ∼30 min at 37 °C. After incubation, the mixture was centrifuged at 3000 rpm for ∼20 min. The obtained supernatant from each reaction mixture was used after centrifugation, and the absorbance was measured at 560 nm using a spectrophotometer. The percentage of hemoglobin denaturation was determined using eq 1.

The purpose of this assay is to evaluate the potential of Ag-NPs to stabilize and lyse HRBC membranes. To do this, we tested the ability of Ag-NPs to inhibit HRBC membrane lysis caused by high temperatures and to detect the amount of hemoglobin released in the samples.

Suspension Preparation for Heat-Induced Hemolysis. The same technique was repeated for blood collection, centrifugation, and washing for heat-induced hemolysis. To prepare a 10% suspension in an isotonic saline solution, an HRBC pellet was used. The reaction mixtures for the control, standard, and test samples were prepared by using the following steps.

(a) The reaction mixture for the negative control was prepared using 0.1 mL of blood suspension (10%), 0.88 mL of PBS, and 0.02 mL of distilled water.

(b) The reaction mixture for the positive control was prepared using 0.1 mL of blood suspension (10%), 0.02, 0.04, 0.06, and 0.08 μg/mL diclofenac sodium, and 0.88, 0.86, 0.84, and 0.82 mL of PBS.

(c) The reaction mixture for the test group was prepared using 0.1 mL of blood suspension (10%), 0.02, 0.04, 0.06, and 0.08 μg/mL Ag-NPs, and 0.88, 0.86, 0.84, and 0.82 mL of PBS.

The reaction mixture was incubated at 54 °C for ∼30 min. Following the incubation, all tubes were cooled by being placed in a container with cool water. Then, centrifugation was performed at 5400 rpm for 5 min, and the resultant supernatant from each sample was collected. The absorbance was measured using a spectrophotometer, and eq 1 was employed to determine the percentage of inhibition of HRBC lysis.

$$\%\ \text{inhibition} = \frac{\text{absorbance of control} - \text{absorbance of sample}}{\text{absorbance of control}} \times 100 \quad (1)$$

Characterizations. Various characterization tools were used to investigate the crystal structure, surface morphology, elemental analysis, and optical spectroscopy of the prepared Ag-NPs. An X-ray diffractometer (Thermo-Scientific instrument, Model: EQUINOX-3000) with a Cu Kα1 radiation source (λ = 1.5406 Å) was used in an ambient environment to record the XRD pattern of the Ag-NP powder sample in the 2θ range varying from 20 to 80°.

Morphological and elemental analyses of the as-synthesized sample were carried out via a field emission scanning electron microscope (TESCAN made, Model: MAIA-3) equipped with an Octane Elite EDS detector. The UV−vis spectrum of the sample was recorded from 200 to 750 nm wavelength via a spectrophotometer (DS5) in a quartz cuvette. Fourier transformed infrared (FTIR, Nicolet 6700 spectrometer) was employed to investigate the chemical bonding in the sample. To analyze the supernatant obtained from each reaction mixture, a spectrophotometer (UV 5100B spectrophotometer) was used for anti-inflammatory activities.

For studying the antibacterial activities of Ag-NPs, four different types of pathogenic Gram-negative bacterial strains,

https://doi.org/10.1021/acsomega.3c09851
ACS Omega 2024, 9, 13208−13216

including *E. coli* (*E. coli*), Klebsiella, Shigella, and Salmonella, were provided by the Department of Biotechnology, and the in vitro anti-inflammatory activity facilities were provided by the Department of Zoology, AWKUM.

RESULTS AND DISCUSSIONS

The X-ray diffraction (XRD) patterns of the prepared Ag-NPs were recorded in an ambient environment in the 2θ range from 20 to 80° and is shown in Figure 2a. The red lines show the peak positions of standard silver XRD data in ICSD Card # 003-0931. There is an excellent match of all peaks with the standard one. All peaks were indexed using the same standard ICSD card. The broadness of peaks shows that the particle size of silver particles is very small. Since there is no extra peak in the XRD pattern of the sample, it indicates the formation of polycrystalline single-phase Ag-NPs. The Bragg's diffraction peaks appeared at positions 38.28, 44.23, 64.5, and 77.4° and were used to calculate different structural parameters. Different relations and models can be used to calculate the average crystallite size (d). Among these, Scherrer's relation only considers the effect of the average crystallite size (D) on Bragg's peak broadening, but it provides no information about the lattice strain (ε). To consider the contribution of both the crystallite size (D) and lattice strain (ε) corresponding to each Bragg peak of Ag-NPs, as denoted by eq 2, modified Williamson−Hall models, such as the uniform deformation model (UDM), uniform stress deformation model (USDM), and uniform deformation energy density model (UDEDM), were used in this study. UDM considers the concept of a consistent lattice strain (ε) in all crystallographic directions, acknowledging the isotropic nature of the crystal. This implies that the material properties remain unaffected by the measurement direction.

$$\beta_{hkl} = [(\beta_{hkl})_D + (\beta_{hkl})_\varepsilon] \tag{2}$$

$$\beta_{hkl}\cos(\theta) = \frac{K\lambda}{D} + 4\varepsilon\sin(\theta) \tag{3}$$

where D is the crystallite size, λ is the X-ray wavelength, β is the fwhm, K is the Debye Scherer's constant, θ is the diffraction angle; likewise, $D = \frac{K\lambda}{\beta_{hkl}\cos(\theta)}$nm and $\varepsilon = \frac{\beta_{hkl}}{4\tan(\theta)}$ show the corresponding contribution to the broadening of Bragg's peaks, respectively, where it was assumed that both had independent contributions and had a Cauchy-like profile. Equation 3 is a straight-line equation known as the UDM equation. Figure 2b shows the UDM plot of the Ag-NPs. The lattice expansion or defects in the Ag-NPs were attributed to the lattice strain development, and its value was calculated from the positive slope of the straight line. In contrast, the intercept gives the value of the average crystallite size (D) of the Ag-NPs.

The UDM model works under the assumption that materials must be homogeneous and isotropic, although this assumption is not applicable to real crystals. The real crystals are anisotropic. Consequently, the W−H equation indicates the relationship between the lattice strain (ε) and Bragg's peak broadening, which must be adjusted to include anisotropic terms. In response, USDM was developed by incorporating an anisotropic strain (ε). In USDM, the lattice deformation stress (σ) is assumed to be uniform in all directions along the lattice planes, encompassing a minor lattice strain (ε).

Hooke's law, which shows a linear relationship between stress and strain mathematically, can be expressed as $\sigma = \varepsilon E_{hkl}$, where E_{hkl} is the Young's modulus, and for a cubic crystal, it is given by eq 4

$$\frac{1}{E_{hkl}} = S_{11} - 2\left[(S_{11} - S_{12}) - \frac{1}{2}S_{44}\right]\cdot \left[\frac{h^2k^2 + l^2k^2 + h^2l^2}{(h^2 + k^2 + l^2)^2}\right] \tag{4}$$

where S_{11}, S_{12}, and S_{44} show three independent elastic compliances and their values are -0.974×10^{-11}, 2.26×10^{-11}, and 2.17×1^{-11}, respectively, for Ag-NPs.[39−42] It gives information about the behavior of deformation under various stress conditions. The elastic compliances are further associated with three independent elastic stiffnesses as

$$S_{11} = \left[\frac{C_{11} + C_{12}}{(C_{11} - C_{12})\bullet(C_{11} + 2C_{12})}\right] \tag{5}$$

$$S_{12} = \left[\frac{-C_{12}}{(C_{11} - C_{12})\bullet(C_{11} + 2C_{12})}\right] \tag{6}$$

$$S_{44} = \frac{1}{C_{44}} \tag{7}$$

The calculated Young's modulus (E_{hkl}) values corresponding to (111), (200), (220), and (311) planes of Ag-NPs are 123.015, 127.25, 127.25, and 126.08 GPa, respectively. Equation 8 depicts the modified W−H equation in terms of stress (σ) known as USDM, and it considers uniform stress in all crystallographic directions.

$$\beta_{hkl}\cos(\theta) = \frac{K\lambda}{D} + \frac{4E_{hkl}}{\sigma}\sin(\theta) \tag{8}$$

Figure 2c shows the USDM plot of Ag-NPs where the sloping plot gives the value of average stress (σ), while the intercept provides the average crystallite size (D) of the Ag-NPs.

The UDM assumes an isotropic nature of the crystals, whereas the USDM assumes a linear relationship between the stress (σ) and lattice strain (ε). However, in real crystals, these assumptions are not entirely valid because of the different defects and dislocations that introduce imperfections in almost every crystal of the materials. Consequently, a different model is required to study the real crystals. To address this, UDEDM was used, which considers the presence of a uniform anisotropic lattice strain (ε) in all crystallographic directions. This consistent anisotropic lattice strain (ε) is attributed to the density of the deformation energy. By incorporating these factors, UDEDM offers a more comprehensive framework for studying real crystals. Again, using Hook's law approximation in terms of energy density (μ)

$$\beta_{hkl}\cdot\cos(\theta) = \frac{K\lambda}{D} + 4\sigma\bullet\sin(\theta)\left[\sqrt{\frac{2\bullet\mu}{E_{hkl}}}\right] \tag{9}$$

Figure 2d depicts the plot of eq 9, known as UDEDM, in which the lattice strain is $\varepsilon = 4\sigma\bullet\left[\sqrt{\frac{2\bullet\mu}{E_{hkl}}}\right]$. The slope of the plot gives the energy density value, while the intercept of the

https://doi.org/10.1021/acsomega.3c09851
ACS Omega 2024, 9, 13208−13216

provides the average crystallite size (D). All the calculated structural parameters are summarized in Table 1.

Table 1. Structural Parameters Calculated from the XRD Analysis

models	crystallite size (nm)	lattice strain (10^{-3})	Young's modulus (GPa)	energy density (μ)	stress (MPa)
UDM	23.06	2.97			371
USDM	23.82	3.14	125		392
UDEDM	23.43	3.05		0.0057	381
Scherer's	20				

Equation 10 was used to calculate the lattice constant (a), which is 4.07 Å, and it is consistent with the standard value of the lattice constant for Ag-NPs.[43]

$$a = d(hkl)\sqrt{(h^2 + k^2 + l^2)}\ \text{Å} \tag{10}$$

where $d(hkl)$ is the interplanar distance and (hkl) is the Miller indices of the plane.

Figure 3a shows the low-magnification micrograph of Ag-NPs taken by a field emission scanning electron microscope. The inset in Figure 3a shows a high-resolution field-emission scanning electron microscopy (FE-SEM) image of the same sample. It is evident from FE-SEM micrographs that Ag-NPs are almost spherical, uniform, and less agglomerated due to the capping agent, PVP, added to the solution during the synthesis process. Figure 3b shows the EDS profile of Ag-NPs, which shows only silver peaks. The low-intensity carbon peak is due to the carbon tap used on the sample holder, or it may be due to the presence of some carbon from precursors on the Ag-NPs surface.

Figure 4a shows the UV−vis absorption spectrum of Ag-NPs. The strong absorption broad peak in the visible region at 427 nm shows the SPR effect of Ag having a small particle size and a spherical morphology. The SPR effect is caused by a collective oscillation of the metallic surface's conduction electrons (plasmons). Due to this phenomenon, Ag-NPs have higher absorption intensities than NPs of other metals of the same size. The optical properties of Ag-NPs might be tailored by controlling their size, morphology, and the local refractive index close to the surface. Thus, eq 11 can be used to calculate the refractive index (n) from the UV−vis absorption

$$n = \frac{1}{T_{ra}} + \sqrt{\frac{1}{(T_{ra}) - (1)}} \tag{11}$$

$$n = \frac{1}{(10^{-A}) \times 100} + \sqrt{\frac{1}{(10^{-A}) \times (100 - 1)}} \tag{12}$$

where T_{ra} and A are the transmittance (%) and the absorbance, respectively. In Figure 4b, it can be observed that the refractive index (n) value of Ag-NPs is 0.135, which is greater than that of AgO and consistent with the actual value of Ag-NPs. It is essential to understand the behavior of the refractive index as a function of energy ($h\nu$) for designing various devices, for example, optical communication devices, plasmonic sensors, light-emitting diodes (LED), and biomedical devices. This allows for the manipulation of light propagation, scattering, and absorption at the mesoscale, creating opportunities for novel optical devices. The band gap energy (E_g) was estimated using Tauc's plot in eq 13.

$$(\alpha h\nu)^2 = A(h\nu - E_g) \tag{13}$$

As can be seen from Figure 4c, the results confirm a direct band gap with an energy value of 2.36 eV, and this indicates that the prepared sample needs less energy to facilitate the electron transitions within the energy bands. Further, the band gap energy (E_g) value is lower than that of AgO and consistent with the previously reported literature.[44,45] The optical conductivity (σ_{opt}) was calculated by employing eq 14

$$\sigma_{opt} = \frac{1}{4\pi} nc\alpha \tag{14}$$

where α, n, and c are the absorption coefficient, refractive index, and speed of light in vacuum, respectively. A material's optical conductivity (σ_{opt}) shows the relationship between the magnitude of the induced electric field (E) and the density of the resultant current when exposed to a specific frequency. Therefore, a material's optical conductivity (σ_{opt}) is influenced by the frequency of the electric field (E). The Drude model is commonly employed to describe optical conductivity (σ_{opt}), encompassing both the contribution of free electrons and the damping effect. Figure 4d shows the optical conductivity (σ_{opt}) response as a function of the energy of the Ag-NPs. The results show high optical conductivity (σ_{opt}) within the range of 10^7 (Ω^{-1} cm^{-1}) and demonstrated a more vital interaction with the incident electromagnetic (EM) waves in the visible portion of the EM spectrum. This strong interaction is mainly due to the presence of conduction electrons (plasmons), which contribute to its strong optical response compared with those of other NPs. Moreover, the remarkable correlation between the size, morphology, and optical properties has shown that Ag-NPs are

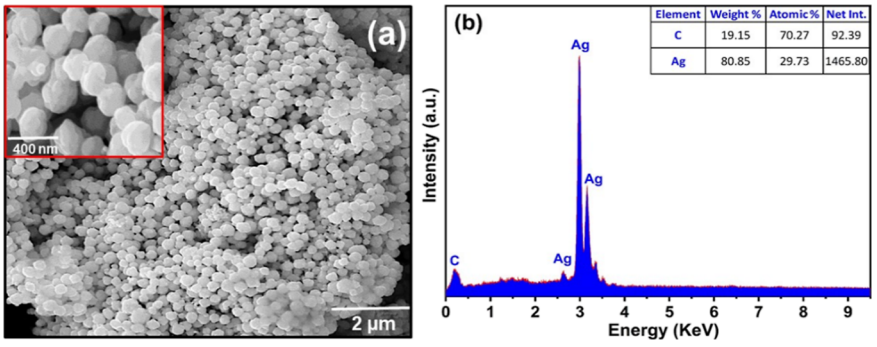

Figure 3. (a) Low- and high-magnification FE-SEM micrographs and (b) EDS spectrum of Ag-NPs.

https://doi.org/10.1021/acsomega.3c09851
ACS Omega 2024, 9, 13208−13216

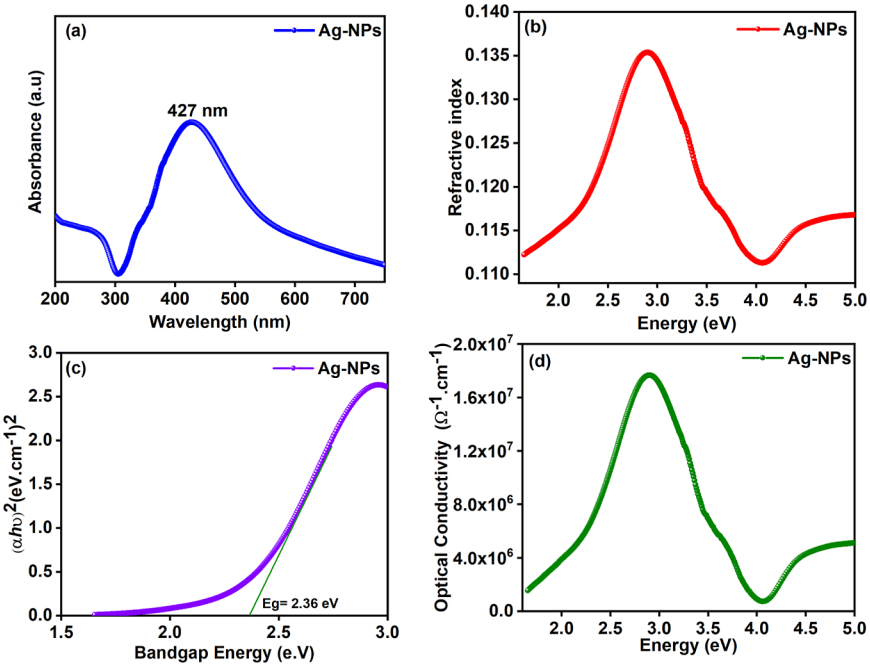

Figure 4. (a) UV−visible spectrum, (b) refractive index, (c) Tauc's plot, and (d) optical conductivity of Ag-NPs.

beneficial in various high-performance applications on the biomedical side.

The FTIR spectrum was recorded from 500 to 4500 cm^{-1}, as shown in Figure 5. The FTIR spectrum also confirmed that

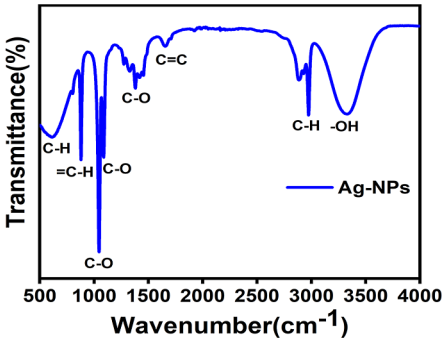

Figure 5. (a) FTIR spectrum of the Ag-NPs.

the prepared Ag-NPs sample is pure. The stretching vibrations at 3328 cm^{-1} show the presence of hydroxyl (−OH) groups at the surface, while the peaks that appeared at 2974 and 2888 cm^{-1} were assigned to the strong stretching vibration of the C−H bond. In the double bond region at 1650 cm^{-1}, weak stretching vibrations of the (C═C) alkene functional group were observed. The stretching peaks at 1380, 1087, and 1045 cm^{-1} represent the C−O bond stretching. Moreover, the bending at 879 and 618 cm^{-1} could be assigned to the (═C−H) and (C−H) alkyne functional groups, respectively. Since no other vibration peaks were found, it suggests that prepared silver is in metallic form with some functional groups attached to the surfaces of Ag-NPs.

The left agar plate in Figure 6a shows Ag-NPs activity against the Klebsiella bacterial strain, while the right one is for two different antibiotics available in the market. Similarly, the left side agar plates in Figure 6b−d show Ag-NPs activities against Shigella, Salmonella, and *E. coli* bacterial strains,

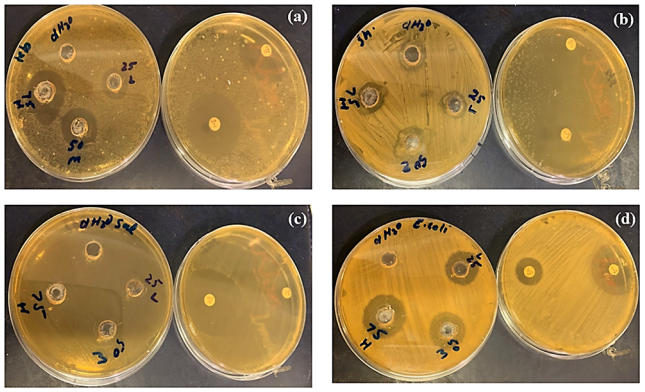

Figure 6. Inhibition zone of Ag-NPs against (a) Klebsiella, (b) Shigella, (c) Salmonella, and (d) *E. coli* bacteria.

respectively, while the right-hand side agar plates in Figure 6b−d show the effect of antibiotics. On the left side of the agar plate are four wells (size around 6 mm). In each figure of Figure 6a−d, one well (on the left side of the agar plate) is left as the positive control well (i.e., only DI is added). In contrast, the remaining three wells show Ag-NPs solutions in DI with different concentrations, i.e., 25, 50, and 75 μg/mL. It is evident from Figure 6a,b,d that Ag-NPs show efficient inhibition against three bacterial strains such as *E. coli*, Klebsiella, and Shigella, while this effect against Salmonella as shown in Figure 6c is almost silent, which may be due to serovars of Salmonella used in the activity. Figure 7a,b shows the zone of inhibition and the effect of Ag-NP concentration on bacterial growth. The size of the inhibition zone was found to increase with increasing Ag-NPs concentration. This indicates that higher concentrations of Ag-NPs are more effective at inhibiting bacterial growth against *E. coli* and Klebsiella. However, in the case of the Shigella bacterial strain, a concentration of 50 μg/mL was found to be the minimum inhibition concentration of Ag-NPs for the minimum bacterial growth. It can be concluded that bacterial growth was slow at

https://doi.org/10.1021/acsomega.3c09851
ACS Omega 2024, 9, 13208−13216

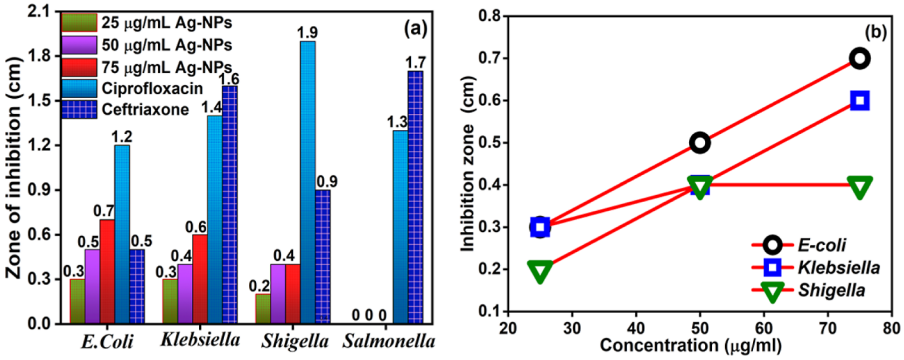

Figure 7. (a) Inhibition zone. (b) Effect of Ag-NPs concentrations on the inhibition zone.

low concentrations of Ag-NPs, and at higher concentrations, the growth was completely inhibited. This indicates that the prepared Ag-NPs are bacteriostatic at a low Ag concentration and bactericidal at a high Ag concentration. The maximum calculated zone of inhibition was 0.7 ± 14, 0.6 ± 16, and 0.4 ± 25% cm for *E. coli*, Klebsiella, and Shigella, respectively.

The in vitro anti-inflammatory activity was assessed using HRBC membrane stabilization and heat-induced hemolysis assays. In HRBC membrane stabilization, we measured the released lysosomal enzymes during inflammation and their contribution to several inflammation-associated diseases. Inhibition of the lysosomal membrane occurs when the drug is used for the treatment of inflammation. Ag-NPs effectively stabilized RBC membranes, which have the same composition as lysosomal membranes, by inhibiting RBC lysis caused by low osmotic pressure. The amount of hemoglobin released was used to determine the RBC membrane stabilization potential of the Ag-NPs, and diclofenac sodium was used as a reference drug.

Various concentrations, 20, 40, 60, and 80 μg/mL, of Ag-NPs were tested, resulting in inhibition of 36.6, 55.5, 61.2, and 59.71%, respectively. For comparison, diclofenac sodium was also tested at the same concentrations and showed inhibition of 47.4, 67.1, 72.1, and 69.8%, respectively. The Ag-NPs showed the lowest percentage inhibition at 20 μg/mL, while the highest percentage inhibition was observed at 100 μg/mL, as shown in Figure 8.

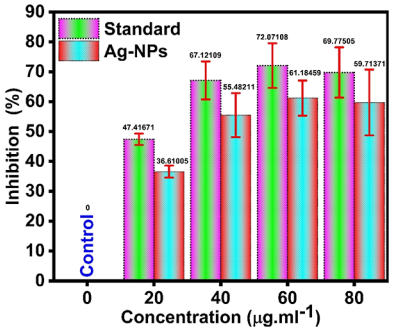

Figure 8. Effect of EGE on the HRBC membrane stabilization assay.

The heat-induced hemolysis is also based on the stabilization and lysis of RBC membranes. HRBC membrane stabilization potential of Ag-NPs was checked in this assay by inhibiting RBC-membrane lysis induced by measuring the hemoglobin content released in the samples, which showed that Ag-NPs effectively inhibited the lysis of RBCs caused by high temperatures, as evidenced by the increasing order of percentage of inflammation inhibition, as shown in Figure 9.

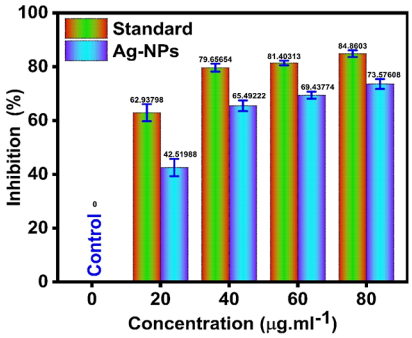

Figure 9. Effect of MGE on the heat-induced hemolysis assay.

Different concentrations of Ag-NPs were used that are 20, 40, 60, and 80 μg/mL, which showed 42.1, 65.1, 69, and 73.6% of inhibition, respectively. The standard drug was put in the standard group as 20, 40, 60, and 80 μg/mL, which showed 62.9, 78.9, 81.2, and 84.7% of inhibition, respectively. The minimum percentage of inhibition was demonstrated at 20 μg/mL, which amounted to 42.12%. On the other hand, the maximum percentage of inhibition was observed at 80 μg/mL, amounting to 73.6%.

CONCLUSIONS

A polyol approach was used for the synthesis of Ag-NPs. A slight modification was incorporated into this technique using a protective agent (PVP), ethylene glycol, and various experimental parameters to obtain Ag-NPs with the desired shape and morphology. The prepared Ag-NPs were uniform, spherical, and less agglomerated. Various characterization techniques have been employed to study the crystal structure, morphology, elemental composition, and optical properties. Different models were used to calculate the structural parameters of the prepared Ag-NPs. The crystallite size and lattice strain values were very close to each other, which demonstrates the accuracy of the different mathematical models. FESEM micrographs showed round, uniformly sized NPs with an average diameter of approximately 200 nm.

In contrast, the EDS profile shows a strong peak at ∼3 keV, which reflects the SPR effect of silver (Ag), and the calculated refractive index (n) and band gap value clearly indicate the formation of Ag-NPs. FTIR spectroscopy results also supported the formation of Ag-NPs. The antibacterial activity of Ag-NPs against Gram-negative pathogenic bacterial strains

https://doi.org/10.1021/acsomega.3c09851
ACS Omega 2024, 9, 13208−13216

such as *E. coli*, Klebsiella, Shigella, and Salmonella has shown efficient inhibition against Gram-negative *E. coli*, Klebsiella, and Shigella. The in vitro, anti-inflammatory activity was tested using HRBC membrane stabilization and heat-induced hemolysis assays, in which the prepared Ag-NPs showed maximum inhibition of 73.6 and 57.9%, in comparison with diclofenac sodium, which showed inhibition of 84.8 and 72.1%, respectively. The anti-inflammatory potential of Ag-NPs was similar to that of diclofenac sodium. Thus, Ag-NPs are effective antibacterial and anti-inflammatory agents that have potential pharmaceutical applications.

■ ASSOCIATED CONTENT

Data Availability Statement

The data used to support the findings of this study are available from the corresponding author upon request.

Supporting Information

The Supporting Information is available free of charge at https://pubs.acs.org/doi/10.1021/acsomega.3c09851.

Details regarding the mechanism of action of Ag-NPs' antibacterial activity, along with a tabulated literature review summarizing antibacterial and anti-inflammatory activities (PDF)

■ AUTHOR INFORMATION

Corresponding Author

Said Karim Shah − *Department of Physics, Abdul Wali Khan University Mardan, Mardan 23200 Khyber Pakhtunkhwa, Pakistan;* orcid.org/0000-0003-0942-2464; Email: saidkarim@awkum.edu.pk

Authors

Ibrar Ahmad − *Department of Basic and Applied Sciences for Engineering, Sapienza University of Rome, Rome 00185, Italy*

Muhammad Nadeem Khan − *Department of Biotechnology, Abdul Wali Khan University Mardan, Mardan 23200 Khyber Pakhtunkhwa, Pakistan*

Khizar Hayat − *Department of Physics, Abdul Wali Khan University Mardan, Mardan 23200 Khyber Pakhtunkhwa, Pakistan;* orcid.org/0000-0001-9472-4947

Tanveer Ahmad − *Department of Physics, Abdul Wali Khan University Mardan, Mardan 23200 Khyber Pakhtunkhwa, Pakistan;* orcid.org/0000-0002-7021-7024

Dilawar Farhan Shams − *Department of Environmental Sciences, Abdul Wali Khan University Mardan, Mardan 23200 Khyber Pakhtunkhwa, Pakistan*

Waliullah Khan − *Department of Chemistry, Abdul Wali Khan University, Mardan 23200 Khyber Pakhtunkhwa, Pakistan*

Vineet Tirth − *Mechanical Engineering Department, College of Engineering, King Khalid University, Abha 61421 Asir, Kingdom of Saudi Arabia; Research Center for Advanced Materials Science (RCAMS), King Khalid University, Abha 61413 Asir, Kingdom of Saudi Arabia;* orcid.org/0000-0002-8208-7183

Gauhar Rehman − *Department of Zoology, Abdul Wali Khan University, Mardan 23200 Khyber Pakhtunkhwa, Pakistan;* orcid.org/0000-0001-8059-9591

Wazir Muhammad − *Department of Physics, Florida Atlantic University, Boca Raton, Florida 33431, United States*

Muawya Elhadi − *Department of Physics, Faculty of Science and Humanities, Shaqra University, Ad-Dawadimi 11911, Saudi Arabia*

Afraa Alotaibi − *Department of Physics, College of Science, Princess Nourah Bint Abdulrahman University, Riyadh 11671, Saudi Arabia*

Complete contact information is available at: https://pubs.acs.org/10.1021/acsomega.3c09851

Notes

The authors declare no competing financial interest.

■ ACKNOWLEDGMENTS

The authors extend their appreciation to the Deanship of Scientific Research at King Khalid University Abha 61421, Asir, Kingdom of Saudi Arabia for funding this work through the Large Groups Project under the grant number RGP.2/545/44.

■ REFERENCES

(1) Choi, H.; Ko, S.-J.; Choi, Y.; Joo, P.; Kim, T.; Lee, B. R.; Jung, J.-W.; Choi, H. J.; Cha, M.; Jeong, J.-R.; et al. Versatile surface plasmon resonance of carbon-dot-supported silver nanoparticles in polymer optoelectronic devices. *Nat. Photonics* **2013**, *7*, 732−738.

(2) Jeong, S. H.; Choi, H.; Kim, J. Y.; Lee, T. W. J. P.; Characterization, P. S. Silver-based nanoparticles for surface plasmon resonance in organic optoelectronics. *Part. Part. Syst. Char.* **2015**, *32*, 164−175.

(3) Amiri, Z.; Malmir, M.; Hosseinnejad, T.; Kafshdarzadeh, K.; Heravi, M. M. Combined experimental and computational study on Ag-NPs immobilized on rod-like hydroxyapatite for promoting Hantzsch reaction. *Mol. Catal.* **2022**, *524*, 112319.

(4) Yu, Y.; Huo, H.; Zhang, Q.; Chen, Y.; Wang, S.; Liu, X.; Chen, C.; Min, D. Nano silver decorating three-dimensional porous wood used as a catalyst for enhancing azo dyes hydrogenation in wastewater. **2022**, *175*, 114268, .

(5) Rahman, N.; Yang, J.; Sohail, M.; Sohail, M.; Khan, R.; Iqbal, A.; Maouche, C.; Khan, A. A.; Husain, M.; Khattak, S. A.; et al. Insight into metallic oxide semiconductor (SnO2, ZnO, CuO, α-Fe2O3, WO3)-carbon nitride (g-C3N4) heterojunction for gas sensing application. *Sens. Actuators, A* **2021**, *332*, 113128.

(6) Khan, R.; Rehman, N. U.; Ilyas, N.; Sfina, N.; Barhoumi, M.; Khan, A.; Althubeiti, K.; Otaibi, S. A.; Iqbal, S.; Rahman, N.; et al. Threshold switching in nickel-doped zinc oxide based memristor for artificial sensory applications. *Nanoscale* **2023**, *15*, 1900−1913.

(7) Siddique, A. B.; Amr, D.; Abbas, A.; Zohra, L.; Irfan, M. I.; Alhoshani, A.; Ashraf, S.; Amin, H. M. Synthesis of hydroxyethylcellulose phthalate-modified silver nanoparticles and their multifunctional applications as an efficient antibacterial, photocatalytic and mercury-selective sensing agent. *Int. J. Biol. Macromol.* **2024**, *256*, 128009.

(8) Zhang, H. *Application of Silver Nanoparticles in Drinking Water Purification*; University of Rhode Island, 2013.

(9) Chen, J.; Xue, Y.; Yang, D.; Ma, S.; Lin, Y.; Wang, H.; Wang, Y.; Ren, H.; Xu, K. Optimizing waste molasses utilization to enhance electron transfer via micromagnetic carriers: Mechanisms and high-nitrate wastewater denitrification performance. *Environ. Res.* **2024**, *242*, 117709.

(10) Zhang, X.; Wang, W.; Wei, D.; Yang, H.; Chen, N.; Wang, Q.; Song, Y.; Ma, Y. Cultivation of the coupling bacteria for simultaneous autotrophic nitrogen and sulfur removal and its remediation effect on the river sediment. *J. Environ. Chem. Eng.* **2024**, *12*, 111923.

(11) Cheng, Z.; Ye, R.; Shi, X.; Lai, C.; Gao, S.; Zhang, D.; Xu, Y.; Wang, C.; Chu, F. A multiple cross-linking strategy to develop an environment-friendly and water resistance wheat gluten protein wood adhesive. *Int. J. Biol. Macromol.* **2024**, *257*, 128712.

(12) Pustovalov, V. K. Heating of nanoparticles and their environment by laser radiation and applications. *Nanotechnol. Precis. Eng.* **2024**, *7*, 015001.
(13) Rahman, A.; Rehman, G.; Shah, N.; Hamayun, M.; Ali, S.; Ali, A.; Shah, S. k.; Khan, W.; Shah, M. I. A.; Alrefaei, A. F. Biosynthesis and Characterization of Silver Nanoparticles Using Tribulus terrestris Seeds: Revealed Promising Antidiabetic Potentials. *Molecules* **2023**, *28*, 4203.
(14) Yi, J.; Li, L.; Yin, Z.-j.; Quan, Y.-y.; Tan, R.-r.; Chen, S.-l.; Lang, J.-r.; Li, J.; Zeng, J.; Li, Y.; et al. Polypeptide from Moschus Suppresses Lipopolysaccharide-Induced Inflammation by Inhibiting NF-κ B-ROS/NLRP3 Pathway. *Chin. J. Integr. Med.* **2023**, *29*, 895−904.
(15) Ahmed, B.; Bilal Tahir, M.; Sagir, M.; Hassan, M. Bio-inspired sustainable synthesis of silver nanoparticles as next generation of nanoproduct in antimicrobial and catalytic applications. *J. Mater. Sci. Eng. B* **2024**, *301*, 117165.
(16) Vadakkan, K.; Rumjit, N. P.; Ngangbam, A. K.; Vijayanand, S.; Nedumpillil, N. K. Novel advancements in the sustainable green synthesis approach of silver nanoparticles (AgNPs) for antibacterial therapeutic applications. *Coord. Chem. Rev.* **2024**, *499*, 215528.
(17) Song, Y.; Nallathamby, P. D.; Huang, T.; Elsayed-Ali, H. E.; Xu, X.-H. N. Correlation and characterization of three-dimensional morphologically dependent localized surface plasmon resonance spectra of single silver nanoparticles using dark-field optical microscopy and spectroscopy and atomic force microscopy. *J. Phys. Chem. C* **2010**, *114*, 74−81.
(18) Millstone, J. E.; Hurst, S. J.; Métraux, G. S.; Cutler, J. I.; Mirkin, C. A. Colloidal gold and silver triangular nanoprisms. *Small* **2009**, *5*, 646−664.
(19) Maillard, M.; Giorgio, S.; Pileni, M.-P. Tuning the size of silver nanodisks with similar aspect ratios: synthesis and optical properties. *J. Phys. Chem. B* **2003**, *107*, 2466−2470.
(20) Wiley, B.; Sun, Y.; Xia, Y. Synthesis of silver nanostructures with controlled shapes and properties. *Acc. Chem. Res.* **2007**, *40*, 1067−1076.
(21) Caswell, K.; Bender, C. M.; Murphy, C. J. Seedless, surfactantless wet chemical synthesis of silver nanowires. *Nano Lett.* **2003**, *3*, 667−669.
(22) Dong, X.; Ji, X.; Wu, H.; Zhao, L.; Li, J.; Yang, W. Shape control of silver nanoparticles by stepwise citrate reduction. *J. Phys. Chem. C* **2009**, *113*, 6573−6576.
(23) Jena, B. K.; Mishra, B.; Bohidar, S. Synthesis of branched Ag nanoflowers based on a bioinspired technique: their surface enhanced Raman scattering and antibacterial activity. *J. Phys. Chem. C* **2009**, *113*, 14753−14758.
(24) Singh, P.; Pandit, S.; Jers, C.; Joshi, A. S.; Garnæs, J.; Mijakovic, I. Silver nanoparticles produced from Cedecea sp. exhibit antibiofilm activity and remarkable stability. *Sci. Rep.* **2021**, *11*, 12619.
(25) Xia, Z.-K.; Ma, Q.-H.; Li, S.-Y.; Zhang, D.-Q.; Cong, L.; Tian, Y.-L.; Yang, R.-Y. The antifungal effect of silver nanoparticles on Trichosporon asahii. *J. Microbiol. Immunol. Infect.* **2016**, *49*, 182−188.
(26) Galdiero, S.; Falanga, A.; Vitiello, M.; Cantisani, M.; Marra, V.; Galdiero, M. Silver nanoparticles as potential antiviral agents. *Molecules* **2011**, *16*, 8894−8918.
(27) Midha, K.; Singh, G.; Nagpal, M.; Arora, S. Potential Application of Silver Nanoparticles in Medicine. *Nanosci. Nanotechnol. - Asia* **2016**, *6*, 82−91.
(28) Zhang, F.; Wu, X.; Chen, Y.; Lin, H. Application of silver nanoparticles to cotton fabric as an antibacterial textile finish. *Fibers Polym.* **2009**, *10*, 496−501.
(29) Yu, Y.; Zhou, Z.; Huang, G.; Cheng, H.; Han, L.; Zhao, S.; Chen, Y.; Meng, F. Purifying water with silver nanoparticles (AgNPs)-incorporated membranes: Recent advancements and critical challenges. *Water Res.* **2022**, *222*, 118901.
(30) Ginwala, R.; Bhavsar, R.; Chigbu, D. I.; Jain, P.; Khan, Z. K. Potential role of flavonoids in treating chronic inflammatory diseases with a special focus on the anti-inflammatory activity of apigenin. *Antioxidants* **2019**, *8*, 35.
(31) Rohini, P.; Aditya, T.; Anil, M.; Arun, K. Anti-inflammatory and antioxidant potentiality of Solanum xanthocarpum. *Afr. J. Biotechnol.* **2018**, *17*, 1188−1195.
(32) Salleh, A.; Naomi, R.; Utami, N. D.; Mohammad, A. W.; Mahmoudi, E.; Mustafa, N.; Fauzi, M. B. The potential of silver nanoparticles for antiviral and antibacterial applications: A mechanism of action. *Nanomaterials* **2020**, *10*, 1566.
(33) Hsueh, Y.-H.; Lin, K.-S.; Ke, W.-J.; Hsieh, C.-T.; Chiang, C.-L.; Tzou, D.-Y.; Liu, S.-T. The antimicrobial properties of silver nanoparticles in Bacillus subtilis are mediated by released Ag+ ions. *PLoS One* **2015**, *10*, No. e0144306.
(34) Wu, Y.; Yang, Y.; Zhang, Z.; Wang, Z.; Zhao, Y.; Sun, L. A facile method to prepare size-tunable silver nanoparticles and its antibacterial mechanism. *Adv. Powder Technol.* **2018**, *29*, 407−415.
(35) Wang, T.; Liu, W. Chronic and transgenerational effects of silver nanoparticles in freshwater gastropod Lymnaea stagnalis. *Chemosphere* **2023**, *313*, 137386.
(36) Le Ouay, B.; Stellacci, F. Antibacterial activity of silver nanoparticles: A surface science insight. *Nano today* **2015**, *10*, 339−354.
(37) Osonga, F. J.; Akgul, A.; Yazgan, I.; Akgul, A.; Eshun, G. B.; Sakhaee, L.; Sadik, O. A. Size and shape-dependent antimicrobial activities of silver and gold nanoparticles: A model study as potential fungicides. *Molecules* **2020**, *25*, 2682.
(38) Jeong, Y.; Lim, D. W.; Choi, J. Assessment of Size-Dependent Antimicrobial and Cytotoxic Properties of Silver Nanoparticles. *Adv. Mater. Sci.* **2014**, *2014*, 1−6.
(39) Hopcroft, M. A.; Nix, W. D.; Kenny, T. W. What is the Young's Modulus of Silicon? *J. Microelectromech. Syst.* **2010**, *19*, 229−238.
(40) Zhang, Y.; Ji, V. General compliance transformation relations for all seven crystal systems. *Sci. China: Phys., Mech. Astron.* **2013**, *56*, 694−700.
(41) Sarkar, S.; Das, R. Shape effect on the elastic properties of Ag nanocrystals. *Micro & Nano Lett.* **2018**, *13*, 312−315.
(42) Zhao, Y.; Liu, K.; Zhang, H.; Tian, X.; Jiang, Q.; Murugadoss, V.; Hou, H. Dislocation motion in plastic deformation of nano polycrystalline metal materials: a phase field crystal method study. *Adv. Compos. Hybrid Mater.* **2022**, *5*, 2546−2556.
(43) Diantoro, M.; Fitrianingsih, R.; Mufti, N.; Fuad, A. *AIP Conf. Proc.* **2014**, *1589*, 257−261.
(44) Aziz, A.; Khalid, M.; Akhtar, M. S.; Nadeem, M.; Gilani, Z.; Asghar, H. U. H. K.; Rehman, J.; Ullah, Z.; Saleem, M. Structural, morphological and optical investigations of siler nanoparticles synthesized by sol−gel auto combustion method. *Dig. J. Nanomater. Biostruct.* **2018**, *13*, 679−683.
(45) Samson, O.; Adeeko, T.; Makama, E. Synthesis and optical characterization of silver nanoparticles (Ag-NPs) thin films (TFs) prepared by silar technique. *Int. J. Curr. Res. Acad. Rev.* **2017**, *5*, 15−24.

https://doi.org/10.1021/acsomega.3c09851
ACS Omega 2024, 9, 13208−13216